Vacuum 233 (2025) 113995

Contents lists available at ScienceDirect

Vacuum

journal homepage: www.elsevier.com/locate/vacuum

Pure copper membranes manufactured by green laser powder bed fusion with varying wall-thickness and building orientation: microstructure, properties, and vacuum tightness performance

Tobia Romano [a,b,*], Andris Ratkus [b], Samira Gruber [c], Matteo Pozzi [d], Hendrik Kos [e], Cedric Garion [e], Samuel Rorison [e], Elena López [c], Toms Torims [b,e], Maurizio Vedani [a]

[a] Department of Mechanical Engineering, Politecnico di Milano, Milan, Italy
[b] Institute of Particle Physics and Accelerator Technologies, Riga Technical University, Riga, Latvia
[c] Fraunhofer Institute for Material and Beam Technology (IWS), Dresden, Germany
[d] Rösler Italiana S.r.l., Concorezzo, Italy
[e] The European Organization for Nuclear Research (CERN), Meyrin, Switzerland

ARTICLE INFO

Handling Editor: Prof. L.G. Hultman

Keywords:
Laser powder bed fusion
Copper
Green laser
Additive manufacturing
Helium leak test
Ultra-high vacuum

ABSTRACT

The design freedom offered by additive manufacturing opens up possibilities for developing novel vacuum electronic devices and radio-frequency components with integrated functionalities. High purity copper is often chosen for these applications because it combines excellent electrical and thermal conductivity. Laser powder bed fusion systems equipped with high-power green laser sources have been developed to enhance the processability of pure copper, which exhibits a low absorption rate for conventional infrared lasers. In this study, pure copper parts manufactured by green laser powder bed fusion were characterized in terms of density, impurity content, and mechanical and physical properties to assess their suitability for ultra-high vacuum applications. Additionally, vacuum membranes were produced with different wall-thicknesses and building orientations and tested for helium leakage with a detection limit of 10^{-10} mbar l s^{-1}. Further microstructural characterization analyses were conducted on the tested membranes to determine the critical parameters influencing their performance in ultra-high vacuum environments, such as effective wall thickness and laser scan length, and establish the current wall thickness limits for pure copper components manufactured by green laser powder bed fusion.

1. Introduction

High purity copper is frequently employed in specialized applications requiring excellent electrical and thermal conductivity. These also include vacuum electronic devices (VEDs) and other radio-frequency (RF) components designed for operation in ultra-high vacuum (UHV) environments [1,2]. To meet their typically severe performance requirements, these devices are often custom-designed and produced in limited series using advanced techniques that involve high precision machining and multi-part assembly, which may result in prohibitive fabrication costs, long lead times, and the need for highly skilled labor [3,4].

Additive manufacturing (AM) has the potential to address these limitations. In AM processes, complex geometries can be realized monolithically by depositing the material layer by layer, thus eliminating the need for laborious assembly operations and avoiding junctions that may be susceptible to vacuum failure during component operation [5]. The design flexibility of AM also enables the development of devices integrating features difficult to fabricate using conventional processes, such as internal cooling systems that can allow for high frequency operation mitigating localized temperature spikes [6]. Additionally, AM is well suited for the production of prototypes and customized parts in limited volumes, as it does not require the use of dedicated tools [7]. In recent years, various AM technologies have been applied to manufacture pure copper parts [8,9]. Among them, laser powder bed fusion (LPBF) has shown the capability of producing parts with mechanical and physical properties comparable to those of conventionally processed copper [10,11]. LPBF systems use a highly

* Corresponding author. Department of Mechanical Engineering, Politecnico di Milano, 34 La Masa, Milan, 20156, Italy.
E-mail address: tobia.romano@polimi.it (T. Romano).

https://doi.org/10.1016/j.vacuum.2024.113995
Received 15 May 2024; Received in revised form 27 December 2024; Accepted 27 December 2024
Available online 28 December 2024

focused laser beam to selectively melt the powder material spread on a building platform, layer after layer. The process is usually conducted in argon atmosphere to prevent material contamination [12]. Laser processing of pure copper poses significant challenges due to the high reflectivity of copper for conventional infrared lasers (~1 μm wavelength) [13], which can result in a severe residual porosity in printed parts due to incomplete melting of the powder material [8]. LPBF machines equipped with high-power infrared and green laser sources have been introduced to enhance the processability of copper. In the former case, the higher power compensates for the low absorbance [14], while in the latter case the system operates at a more efficient wavelength (~515 nm), providing a higher absorption rate [13].

Although LPBF has experienced a rapid expansion across various industrial sectors in recent years, its application in the vacuum field is still limited [4]. This is primarily due to the stringent requirements in terms of leak tightness, outgassing control, and surface contamination, particularly critical for UHV applications. The relatively high surface roughness of additively manufactured parts (7–20 μm in PBF processes [12]) has typically been associated with intense outgassing, due to the increased surface area for the adsorption of volatile species [15]. In addition, residual porosity, which is often observed in printed parts, may cause vacuum degradation due to evacuation of trapped gases [16,17]. During the deposition process, pores can both originate from the incorporation of inert shielding gas into the molten pools and from incomplete melting of the powder material [12]. These defects are denoted as gas-induced and lack of fusion porosity, respectively.

Despite these challenges, several studies have suggested the UHV compatibility of LPBF [18,19]. The surface roughness of as-built devices, including vacuum tubes and chambers [16,20–22], did not result in a significant deterioration of the outgassing performance compared to the post-processed counterparts with improved surface finish. The feasibility of reusing the collected excess powder in subsequent printing cycles without compromising material cleanliness was also demonstrated through outgassing tests and residual gas analysis performed on Ti6Al4V specimens [23]. However, this finding cannot be readily translated to pure copper, since a heavily oxidized recycled powder may result in parts with unsatisfactory electrical and thermal properties, as well as suffering from structural defects such as intergranular cracks due to oxide segregation at grain boundary regions and porosity induced by thermal degradation and vaporization of the surface oxide layer found on the powder particles [24]. Regarding pure copper components operating in vacuum, pump down tests were conducted on additively manufactured electrodes installed in a pulsed high-voltage DC system for breakdown dielectric testing [25]. In the first run, a gap distance of 270 μm was set between the anode and the cathode in the system, and a vacuum level of $3 \cdot 10^{-8}$ mbar was achieved after 55 h pump down. In the second repetition, a vacuum level of $2 \cdot 10^{-8}$ mbar was achieved in 3 h with a gap distance of 115 μm. Promising outgassing and helium leak measurements were also performed on pure copper samples manufactured by electron beam powder bed fusion (EB-PBF) [5,26], which uses a high-energy electron beam to selectively melt the powder material deposited in a layerwise fashion [8].

Specific investigations of the UHV performance of pure copper processed by LPBF have not yet been reported in the literature to the authors' knowledge. The present study aims to address this gap to promote the integration of LPBF into the manufacturing practices of pure copper components operating in UHV. Pure copper samples were initially fabricated by LPBF using a green laser source and characterized to assess the material compatibility with UHV in terms of density, chemical purity, and mechanical and physical properties. Subsequently, membranes for helium leak testing were manufactured with different thicknesses and building orientations to establish the wall thickness limits for high purity copper parts produced by LPBF.

2. Materials and methods

Specimens for characterization analyses (Fig. 1(a)) were manufactured by Trumpf using a TruPrint 1000 Green Edition machine equipped with a TruDisk 1020 green laser source with 515 nm wavelength. A gas atomized pure copper powder (m4p™ PureCu, >99.95 % Cu) with 10–45 μm particle size was employed as feedstock material. The process parameters were selected based on previous investigations [11,27,28] and are reported in Table 1, where the linear energy density is defined as the ratio between the laser power and the laser scanning speed. Argon was continuously supplied to the printing chamber to keep the oxygen level below 100 ppm.

The oxygen content in the printed parts was measured with a Leco RO-116 analyzer, while the possible presence of oxide phases was examined by performing X-ray diffraction (XRD) with Co Kα radiation employing a Bruker D8 Advance diffractometer. The hydrogen content was determined through thermal desorption spectroscopy using a Bruker G8 Galileo device. For the analysis, six samples of ~1 g were extracted from the printed bars and sanded with a 320-grit SiC abrasive paper to remove any surface contamination. In each test repetition, the material was melted inside a graphite crucible, while the flow of desorbed hydrogen was continuously monitored with a thermal conductivity detector. Other elements were detected using an ARL iSpark 8860 Thermo Scientific optical emission spectrometer. Qualitative observation of as-built surfaces was conducted using a Zeiss Sigma 500 field-emission scanning electron microscope (FE-SEM). The density of the printed parts was determined through Archimedes' method, using a Mettler Toledo scale filled with distilled water at 20 °C. Sections for microstructural analysis were cut along and perpendicular to the building (z) direction (Fig. 1(b)) and polished to mirror finish following standard metallographic procedures. A Nikon Eclipse LV150NL optical microscope was used to collect micrographs for image analysis with ImageJ software to estimate the fraction of residual porosity. Subsequent chemical etching was performed using a solution prepared with 2.5 g $FeCl_3$, 4 ml HCl, and 50 ml water. Vickers microhardness measurements were conducted with a Future-Tech FM-700 testing machine, applying a load of 50 g for a dwell time of 15 s in the specimen core region across ten test repetitions (BS EN ISO 6507–1:2023). A SIGMATEST 2.069 device based on the eddy current method was used to measure the electrical conductivity along planes parallel and normal to the building (z) direction to evaluate possible effects of the microstructural anisotropy (Fig. 1(c)). Measurements were initially performed on samples in as-built surface condition and then repeated after grinding the parts with a 120-grit SiC abrasive paper to remove the outer porous layer and achieve a surface roughness of ~2 μm [29], thus ensuring a more accurate estimate of the bulk conductivity of the material. Five values were collected for each direction and surface condition, employing an operating frequency of 120 kHz. Since the accuracy of eddy current testing can be affected by edge effects in relatively small parts, additional measurements were performed on a reference annealed pure copper sample (>99.99 % Cu) cut from a wrought bar of similar dimensions (~15 mm diameter) for comparison purposes. Laser flash analysis (LFA) was conducted to determine the thermal diffusivity according to ASTM E1461-13. Disks with 12.7 mm diameter and ~1.5 mm thickness were extracted by electrical discharge machining (Fig. 1(a)), with the thickness parallel to the z and x directions, as illustrated in Fig. 1(b). Both faces of the specimens were polished up to 6 μm diamond suspension and subsequently covered with a thin graphite layer to ensure absorption of the laser beam energy during testing. A reference sample cut from the annealed pure copper bar was prepared following the same procedure. The measurements were conducted with a Linseis LFA 1000 machine operating in vacuum ($\sim 1.2 \cdot 10^{-2}$ mbar), employing a 350 V laser voltage and 1 ms laser pulse duration. A heating ramp of 5 °C min^{-1} was set to collect thermal diffusivity values from room temperature to 450 °C, with three measurements taken every 25 °C, with a tolerance of ±7 °C.

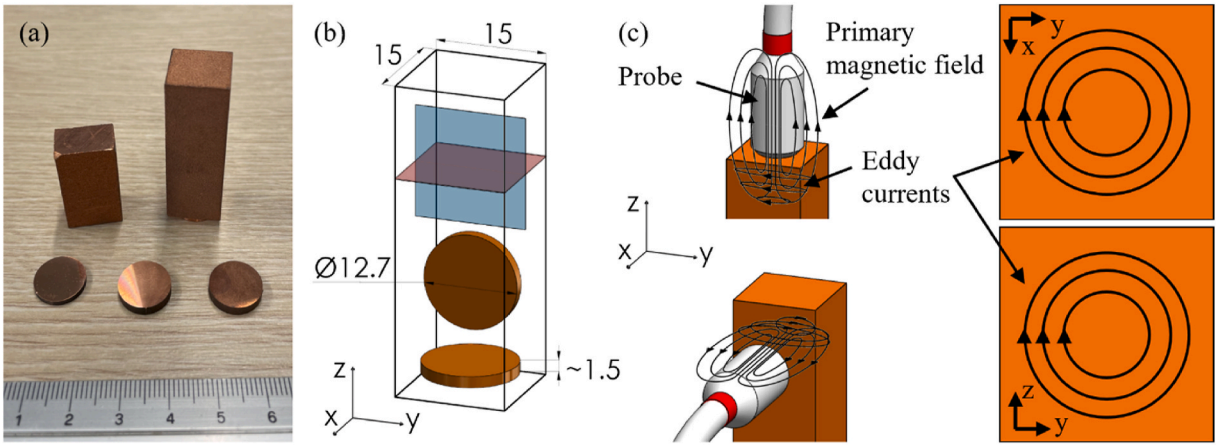

Fig. 1. View of the specimens used for analyses (a), definition of cross-sectional planes and sample orientation for LFA (b), and schematics of measurements of the electrical conductivity along planes parallel and normal to the building (z) direction (c).

Table 1
Process parameters used to manufacture characterization samples and membranes for helium leak testing.

Parameter	Value
Laser power	485 W
Laser scanning speed	600 mm s^{-1}
Layer thickness	30 μm
Linear energy density	0.8 J mm^{-1}
Laser spot diameter	200 μm
Hatch spacing	120 μm

Thin membranes for helium leak testing were manufactured using the same LPBF setup and printing parameters as for the initial characterization samples (Table 1). In this iteration, a gas atomized electrolytic tough pitch (ETP, 99.97 % Cu) copper powder with mostly spherical morphology (Fig. 2(a)) was employed. The particle size and shape characteristics of the powder are shown in Fig. 2(b) and Table 2, along with the oxygen, hydrogen, and nitrogen content measured with an inductar® ONH cube analyzer. This feedstock material exhibited a purity level and particle size distribution comparable to the mp4™ PureCu powder used for the fabrication of characterization samples, allowing the data obtained from the first set of samples to be extended to the series of membranes printed under the same process conditions.

The design of the membranes features a DN 40 ISO-KF type sealing flange, as shown in Fig. 3(a). Membranes with different nominal thickness (2.5, 2, 1.5, 1, 0.75, and 0.5 mm) were printed in three different orientations relative to the building direction for each thickness value (45°, 67°, and 90°, respectively, as illustrated in Fig. 3(b and c)). After printing, the parts were detached from the building plate and the support structures were removed. The flange surface was machined to ensure tightness during subsequent leakage tests (Fig. 3(d)).

Table 2
Particle size, shape characteristics, and oxygen, hydrogen, and nitrogen content of the ETP copper powder.

D10	D50	D90	Sphericity	O	H	N
20.5 μm	27.6 μm	37.1 μm	0.92	230 ppm	10 ppm	30 ppm

Helium leak tests were conducted at room temperature with a Leybold Phoenix 300i equipment, integrating a leak detection system based on a mass spectrometer. A schematic of the experimental setup is depicted in Fig. 4(a). In this configuration, the test membrane is clamped to a standard DN-25 vacuum connector installed at the inlet of the leak detector (Fig. 4(b)). The volume below the membrane is first pumped down to 10^{-3} mbar. When the leak background is below the detection limit set for the test (10^{-10} mbar l s^{-1}, according to CERN requirements for the qualification of vacuum components [30]), helium is injected into the small enclosure above the membrane for ~30 s to achieve a He concentration close to 100 %. The detector records the helium leak rate when it exceeds the threshold value of 10^{-10} mbar l s^{-1} due to the presence of a leak in the membrane. If no signal is recorded, the part is considered vacuum tight.

Following leak testing, the membranes with 1, 0.75, and 0.5 mm thickness were sectioned and prepared for microscopy inspection following the same metallographic procedures described above. Additional manual and vibratory polishing were conducted for electron back scattered diffraction (EBSD) analyses using a 0.03 μm silica colloidal suspension. Chemical etching was performed diluting the initial solution with distilled water at 1:10 ratio. Local thickness tool in ImageJ software was used to measure the actual wall thickness of the sectioned parts to

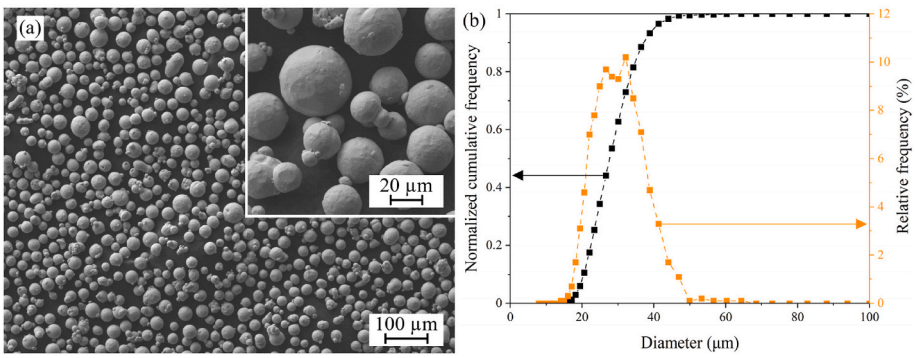

Fig. 2. SEM images (a) and particle size distribution (b) of ETP copper powder used to manufacture membranes for helium leak testing.

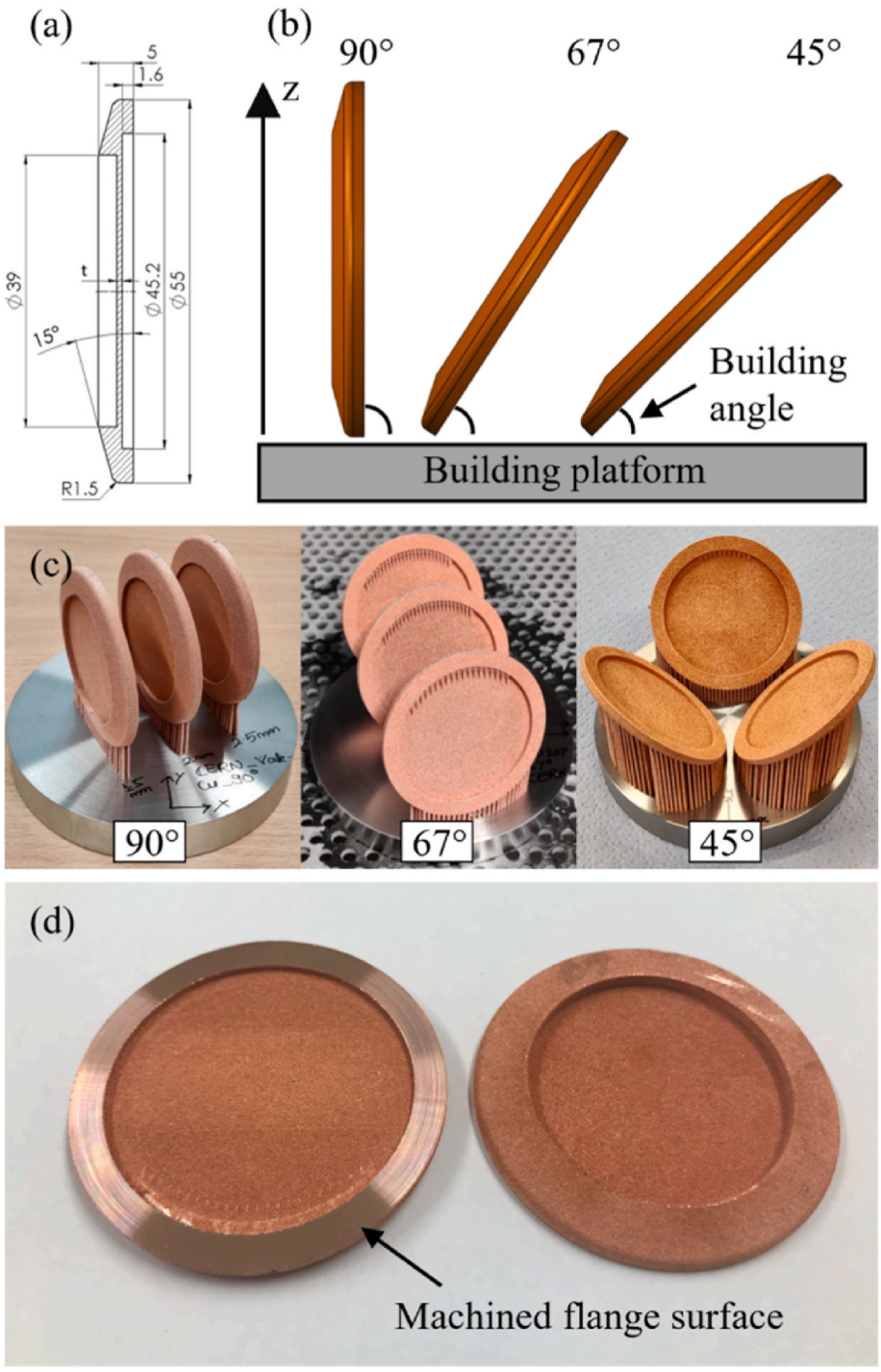

Fig. 3. Membrane design with DN40 ISO-KF sealing flange (a), schematic of building orientations (b), and view of additively manufactured membranes on the building plate (c) and after flange surface machining (d).

compare it with the nominal value and evaluate possible effects of building orientation on the dimensional accuracy. An example of the measurement procedure is shown in Fig. 5.

3. Results and discussion

3.1. Characterization of LPBF specimens

Fig. 6 shows the surface appearance of LPBF specimens. It should be noted that the samples were observed right in as-built conditions. Indeed, they were not subjected to any usual cleaning procedures after printing, such as through manual brushing or compressed air [31], to study their surface characteristics under actual as-built conditions. Despite the use of a smaller hatch spacing compared to the laser spot size (see Table 1), only partially overlapping scanning tracks are visible on the upper surface of the samples, with unmelted particles filling the interstices between adjacent tracks (Fig. 6(a)). This is attributable to the limited thermal input provided to the last deposited layer, which did not receive additional heat from subsequent layers and experienced rapid heat dissipation into the underlying consolidated material. As a result, the deposited tracks may have solidified without the opportunity of fully merging with adjacent and underlying tracks. On the other hand, the

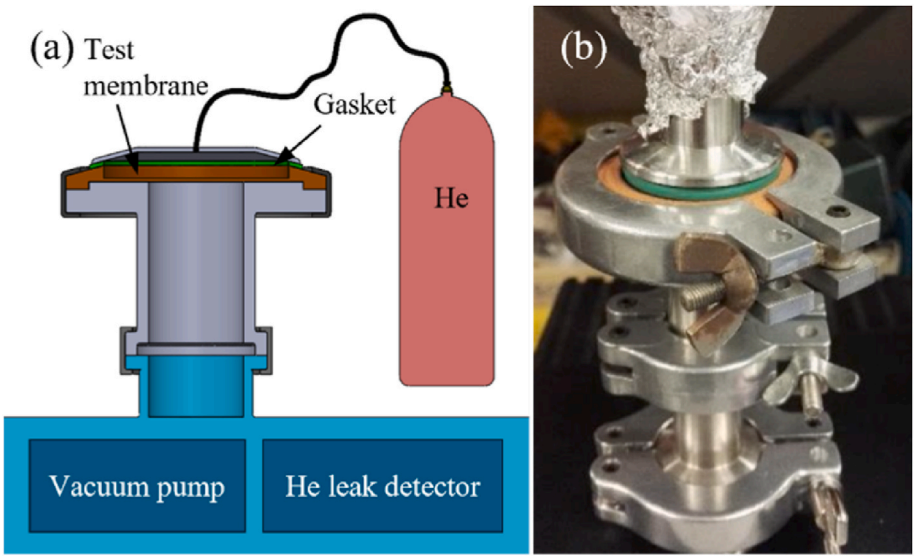

Fig. 4. Schematic of helium leak test setup (a) and view of clamped test membrane (b).

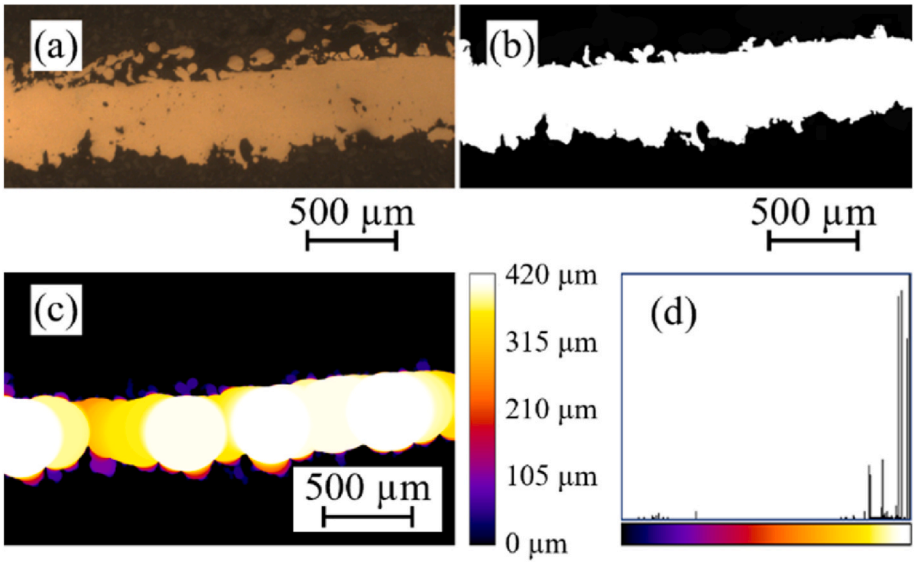

Fig. 5. Example of average thickness measurement on membrane printed with 0.5 mm nominal thickness and 45° building orientation using Local thickness tool in ImageJ software: original cross-section micrograph (a), 8-bit image (b), thickness map (c), and thickness distribution (d).

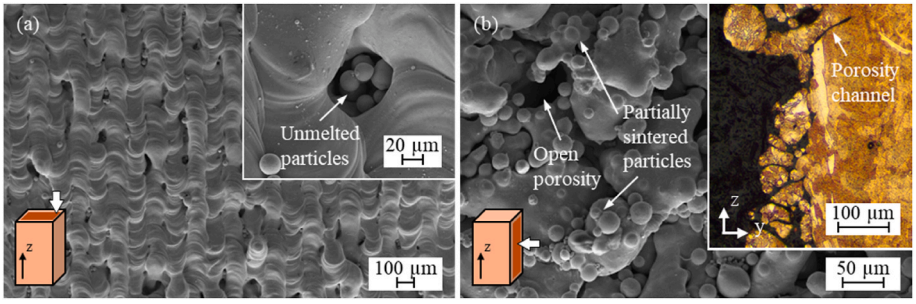

Fig. 6. Surface morphology of as-built specimens in the top (a) and lateral surface (b).

bulk regions of the samples do not display a significant porosity content potentially caused by insufficient track overlapping (Fig. 7). This suggests that the additional heat absorbed from the successive deposited layers contributed to the complete merging of tracks and the healing of possible defects present in the inner regions of the printed parts [32]. The lateral surfaces of the specimens exhibit a large amount of partially melted particles, as evidenced in Fig. 6(b). This feature is typical of parts produced by LPBF, because particles from the powder bed in contact

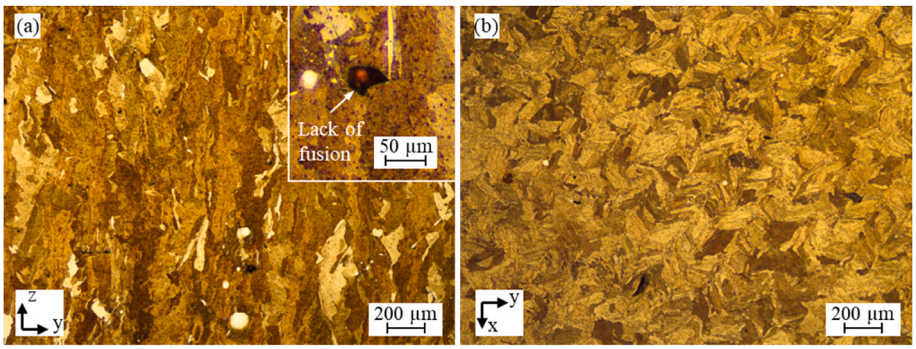

Fig. 7. Microstructure of LPBF specimens along the building (a) and transversal direction (b).

with the consolidated material at high temperature tend to adhere and sinter onto its surface [33]. Irregularly shaped open pores can also be observed, along with occasional elongated porosity channels ~5 µm in diameter and extending 20–80 µm below the surface, as highlighted in the inset of Fig. 6(b). The significant fraction of open porosity, estimated as 6.7 ± 0.6 % through image analysis, may be attributed to the relatively high scanning speed employed in the LPBF process, which resulted in a short interaction time between the laser beam and the melt pool, preventing the molten material from distributing evenly in the surface regions of the samples [34]. The prominent defects observed on both the upper and lateral surfaces of the specimens indicate that a specific set of printing parameters could be further optimized for the surface regions, considering the reduced thermal input compared to the bulk regions, which are reheated and partially melted during the deposition of the successive tracks within and across layers.

The microstructure of the material consists of elongated grains oriented parallel to the building direction (Fig. 7(a)), as typically found in parts manufactured via LPBF [12]. Fig. 7(b) shows the transversal cross section of the grains in the xy plane, highlighting the microstructural anisotropy resulting from the layerwise building process. Occasional lack of fusion defects were observed in the samples, as shown in the inset of Fig. 7(a). The fraction of residual porosity determined by analyzing the micrographs collected in the core region of the samples is ~0.18 %, as reported in Table 3. The density measured by Archimedes' method (~99.34 %) is slightly lower than that estimated by image analysis due to the presence of a surface porous layer of ~200 µm, as highlighted in the inset of Fig. 6(b). The results of chemical composition analyses are provided in Table 4. The oxygen content measured in the samples (~440 ppm) is comparable with that specified in the powder feedstock, indicating that no significant contamination occurred during the printing process. Faint peaks corresponding to Cu_2O oxide can be observed in the XRD pattern shown in Fig. 8. Cu_2O formation at the grain boundary regions can be attributed to oxygen exceeding the solubility limit for copper at room temperature (~2 ppm [3]) and may be responsible for the higher microhardness measured in the printed specimens (75.5 ± 3.2 $HV_{0.05}$) compared to annealed oxygen-free high conductivity (OFHC) copper [35]. This value is also comparable with that found by Yan et al. [36] in copper parts fabricated by LPBF employing a feedstock with similar purity level. Zinc was also detected at a concentration of ~111 ppm, while other elements are present in trace amounts. A low hydrogen content of ~2.5 ppm was measured in thermal spectroscopy analyses.

The results of electrical conductivity measurements are depicted in Fig. 9(a). Values are also expressed with reference to the International Annealed Copper Standard (58 MS m^{-1} = 100 % IACS) and compared to the electrical conductivity of the reference material to account for possible errors due to the small size of the tested parts. Samples in as-built surface condition exhibited a relatively low electrical conductivity, especially along the yz plane (~40 % IACS). This can be attributed to the presence of a porous layer on the vertical surfaces of the printed parts (see inset of Fig. 6(b)), on which the probe was applied to measure the electrical conductivity along the building direction, as schematically shown in Fig. 1(c). The thickness of this layer, rich in pores filled with air and thus acting as an insulator [11], is of the same order of magnitude as the penetration depth of eddy currents, which can be estimated as

$$\delta = \frac{660}{\sqrt{f \times \sigma}} \quad (1)$$

where δ is the penetration depth in mm, f is the test frequency in Hz, and σ is the electrical conductivity of the material expressed as % IACS [11]. After removing the external porous layer, the electrical conductivity increased to approximately 100 % IACS, close to the value measured for the reference sample. The material exhibited a slightly lower conductivity along the transversal direction compared to the building direction. This effect was attributed to the relatively higher density of grain boundaries in the xy plane (Fig. 7(b)), which act as scattering sites for electrons, thereby reducing the electrical conductivity [37]. On the other hand, the elongated grains aligned along the direction of the electric current (Fig. 7(a)) promote the flow of conduction electrons.

Regarding thermal diffusivity, the slightly lower values measured along the transversal direction compared to the building direction (Fig. 9(b)) can also be attributed to the greater abundance of interfaces within the xy planes, which reduce the mean free path of electrons and hinder heat transfer through the material [38]. However, both curves approximately overlap with that of the reference sample and display the typical decreasing trend with temperature [39].

3.2. Helium leak testing and membrane analysis

Table 5 reports the outcomes of helium leak testing. The helium signal read by the detector is indicated for the membranes that exhibited a leak rate above the detection limit of the device, as documented in Ref. [40].

Among the eighteen membranes tested, three did not meet the tightness requirements, displaying leak rates that can be classified, in descending order, as water-, vapor-, and virus-tight, respectively, according to standard criteria based on the typical size of common reference objects [41]. Samples with nominal thickness down to 1 mm are leak tight for all building angles. In the membranes that did not pass the leak test, it can be observed that leakage becomes more severe with decreasing the nominal thickness, because even minor defects, such as the gas-induced and lack of fusion pores highlighted in Fig. 10, can account for a significant fraction of the narrow barrier. Grinschek et al. [42] observed a similar trade-off between material thickness and defect

Table 3
Porosity fraction and density of LPBF samples.

Porosity fraction	Density	Relative density
0.18 ± 0.11 %	8.90 ± 0.02 g cm^{-3}	99.34 %

Table 4
Chemical composition (in ppm) of LPBF specimens.

O	H	Zn	Si	Ag	Pb	Fe	Bi	Sb	S	Cu
442 ± 37	2.5 ± 0.2	111 ± 4	23 ± 9	12 ± 1	12 ± 2	9 ± 7	6 ± 1	6 ± 1	6 ± 1	Balance

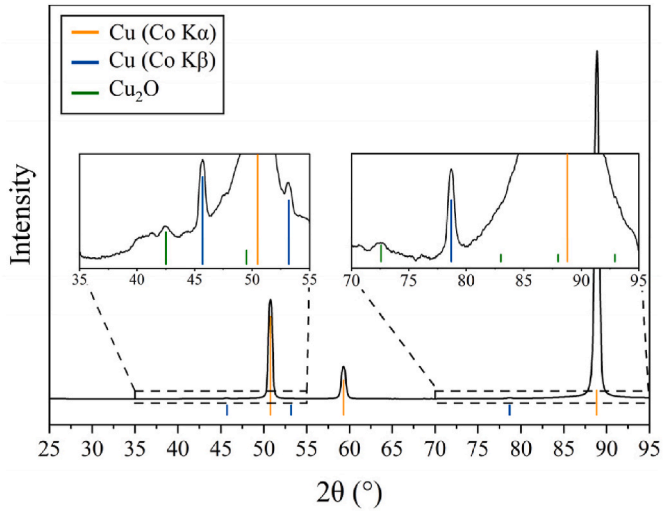

Fig. 8. XRD pattern of LPBF specimens, with peaks corresponding to Cu_2O phase highlighted in the insets.

density in 316L thin-walled parts produced by LPBF. In general, copper experiences inherent helium permeation because the helium molecule is smaller than the lattice spacing of copper. However, the measurement neglects this contribution, taking into account only leakage caused by defects in the material [41]. The helium flow due to the entire defect population in the specimens investigated can be attributed to a single virtual hole of equivalent diameter

$$d \approx \sqrt{q_L} \cdot 10^2 \tag{2}$$

where d is expressed in μm and q_L is the measured leak rate in mbar l s^{-1} [41,42]. Therefore, the three membranes that did not pass the leak test feature an equivalent defect size of ~0.1, ~5, and ~22 μm, respectively, in ascending order of leak rate.

The experimental results indicate that building orientation also plays a role, as it determines both the actual part thickness, as discussed below, and the extent of the area that is scanned by the laser to obtain the designed wall thickness [43]. The scanning length s can be calculated as

$$s = \frac{t}{\sin \vartheta} \tag{3}$$

where t is the nominal wall thickness and ϑ is the building angle, as defined in Fig. 3(b). For 90° building angle, the scanning length corresponds to the part thickness. On the other hand, for lower building angles the scanning length becomes larger than the wall thickness and it increases with increasing part inclination during printing, as schematically shown in Fig. 11. A larger scanning length can potentially improve the quality of the deposited material by reducing the relative weight of the porous and defect-rich outer layer on the overall wall thickness.

The thickness values determined by image analysis of cross-sectional micrographs of the membranes are reported in Table 6. The data show deviations from the nominal thickness exceeding 30 % in most cases, except for membranes manufactured with 45° orientation. Notably, deviations larger than 50 % were observed in vertically printed

Table 5
Results of helium leak testing. The test is considered passed (PASS) if the helium leak rate is lower than the detection limit (10^{-10} mbar l s^{-1}) [40].

	Helium leak rate (mbar l s^{-1})		
Building angle / Nominal thickness (mm)	45°	67°	90°
2.5	PASS	PASS	PASS
2	PASS	PASS	PASS
1.5	PASS	PASS	PASS
1	PASS	PASS	PASS
0.75	PASS	PASS	$1.0 \cdot 10^{-6}$
0.5	PASS	$2.5 \cdot 10^{-3}$	$5.0 \cdot 10^{-2}$

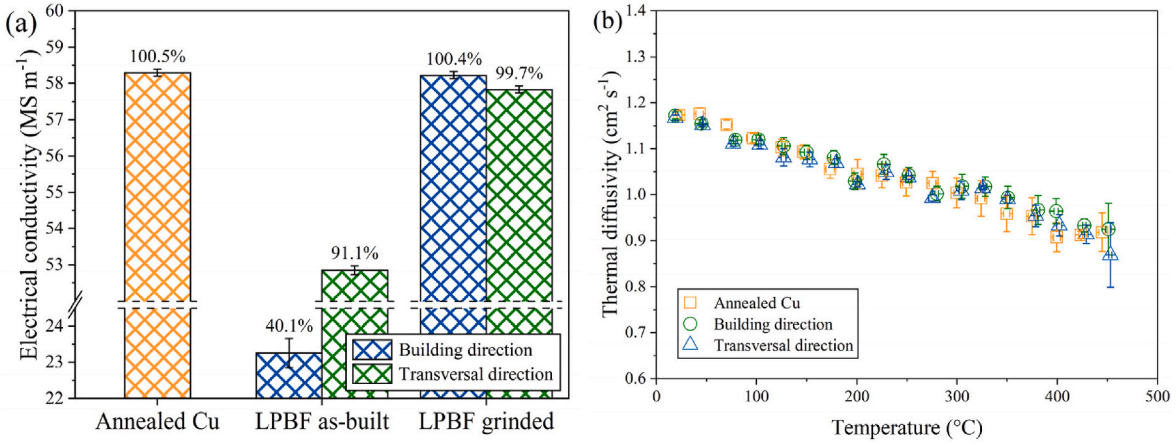

Fig. 9. Electrical conductivity (a) and thermal diffusivity (b) measured along building and transversal directions. Electrical conductivity values are also given in IACS%.

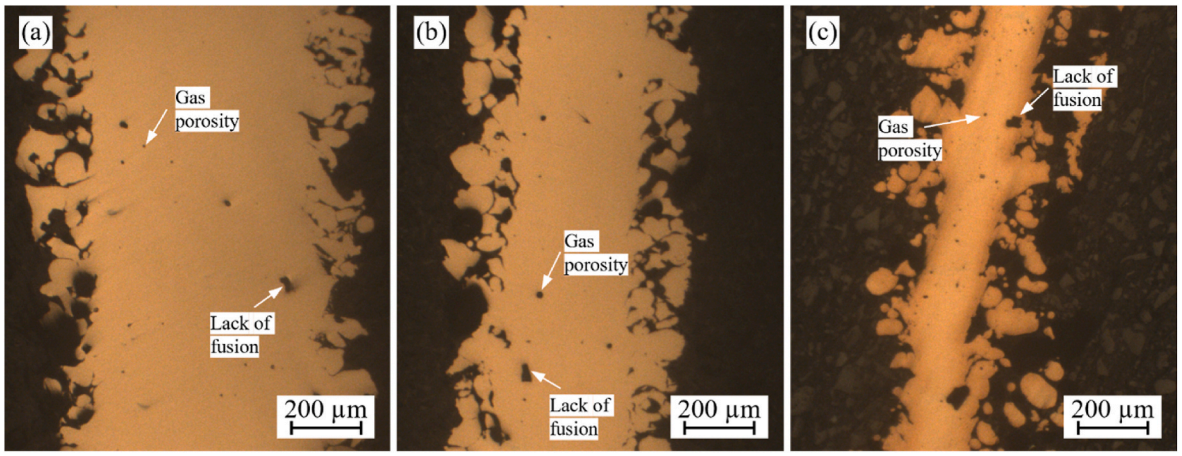

Fig. 10. Lack of fusion and gas-induced porosity observed in membranes manufactured with 90° building angle and nominal thickness of 1 mm (a), 0.75 mm (b), and 0.5 mm (c).

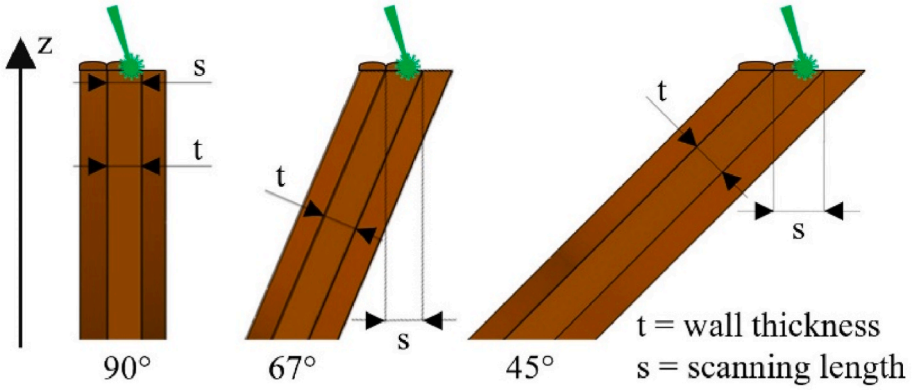

Fig. 11. Schematic illustration of scanning length as a function of the building angle.

Table 6
Average thickness of additively manufactured membranes measured through image analysis.

	Measured thickness (µm)		
Building angle / Nominal thickness (µm)	45°	67°	90°
1000	727 ± 68	694 ± 52	693 ± 51
750	654 ± 69	504 ± 55	363 ± 16
500	383 ± 32	309 ± 38	172 ± 19

membranes with nominal thicknesses of 0.75 and 0.5 mm, which experienced helium leakage. Gruber et al. [11] reported significantly lower dimensional deviations (~3–4%, regardless of the feature nominal size) in thin vertical walls produced using the same experimental setup. This discrepancy may be attributed to the different criteria used for evaluating the dimensions. While Gruber et al. [11] performed 3D scanning measurements to assess the geometrical accuracy of as-printed structures, in the present study the effective thickness of the membranes was determined by considering only the compact core, excluding the porous outer layers consisting of small individual features that do not contribute to preventing helium flow during leak testing. This suggests that previous results cannot be readily generalized to thin-walled structures intended for UHV applications. Dimensional deviations arising from the LPBF process should be carefully considered during the design stage. The processing parameters would also require further optimization to limit the contribution of the porous surface layer to the overall part thickness.

From Tables 6, it can be noted that the effective thickness of the membranes increases with the inclination of the part relative to the building direction, i.e., moving from 90° to 45° building angle. The thickening of inclined walls results from the staircase effect [43], which originates from the discretization of the ideal inclined surface profile with discontinuous steps, each corresponding to one deposited layer. Furthermore, the progressively longer scanning length enabled by larger inclinations (while still within the operational constraints of LPBF technology) potentially allows obtaining a greater thickness of compact material, as discussed earlier.

Fig. 12 shows the microstructure of the additively manufactured membranes. As previously noted in Fig. 7, grains are mostly aligned along the building direction for all different part orientations. This is also evidenced in the inverse pole figure (IPF) maps. The poor indexing observed in some IPF images (e.g., in Fig. 12(c)) can be attributed to an imperfect surface preparation of the samples, probably caused by the release of fine graphite particles from the conductive resin used to embed them during polishing operations. A marked difference in grain size can be noticed between the membranes of 0.5 mm nominal thickness manufactured with different orientations. The part printed with 45° building angle is composed of relatively finer grains, which are generally associated with reduced risk of leaks [44]. On the other hand, in

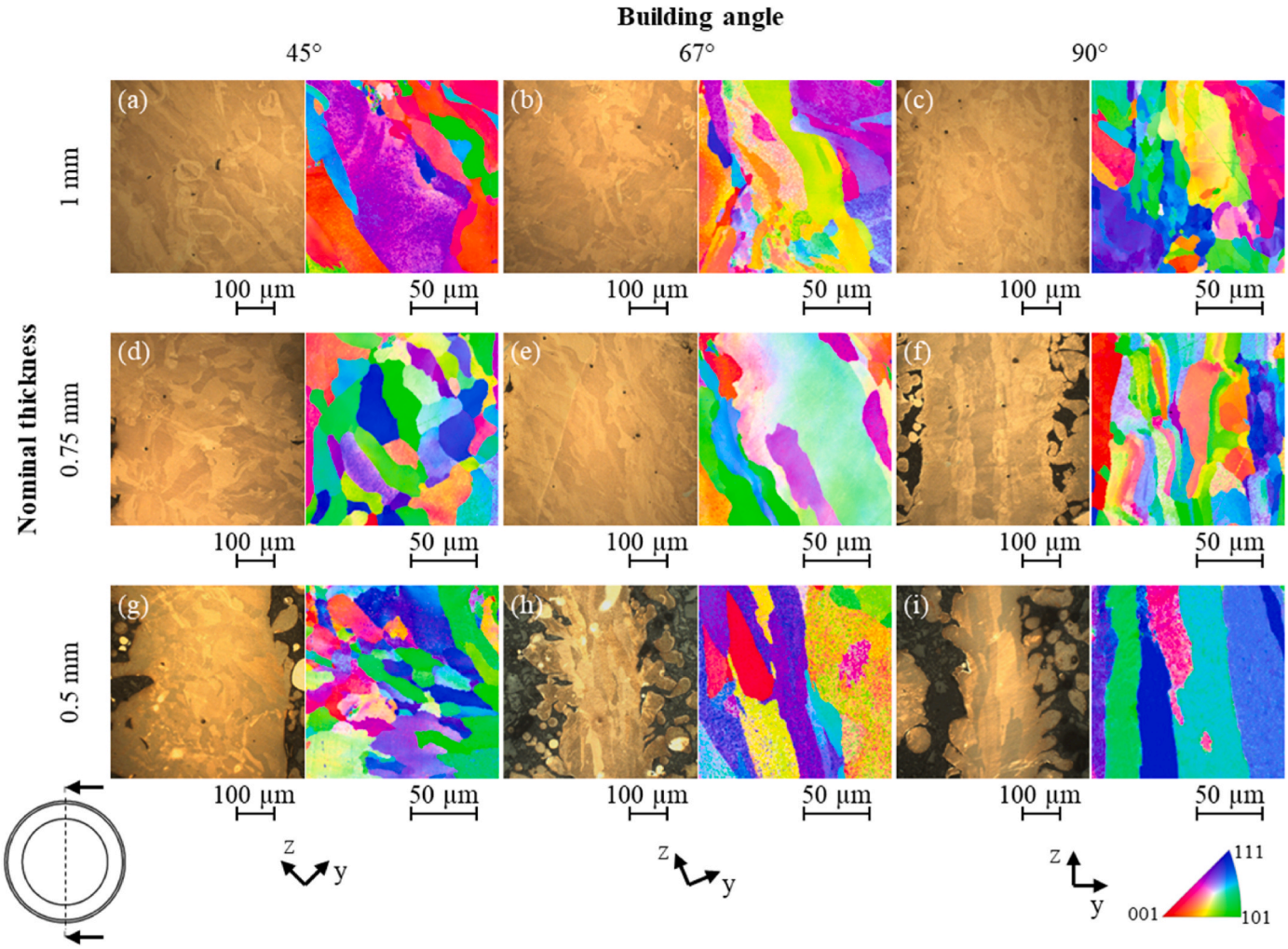

Fig. 12. Optical micrographs and IPF maps of membranes manufactured with different building orientation and nominal thickness.

membranes printed at 67° and 90° inclinations, the entire thickness consists of few large columnar grains. This suggests that coarse columnar microstructure, in combination with low effective thickness, may increase the likelihood of leakage due to the presence of even minor defects in the material.

4. Conclusions

In this work, the characteristics of pure copper parts fabricated by laser powder bed fusion using a green laser source were investigated to assess their suitability for ultra-high vacuum applications. Membranes with varying nominal thickness (0.5–2.5 mm) and building orientation (45°, 67°, and 90°) were also manufactured and tested for helium leakage with 10^{-10} mbar l s^{-1} detection limit.

As-printed parts were almost fully dense and exhibited an oxygen content comparable to the feedstock material and a negligible hydrogen content, indicating that no significant bulk contamination occurred during the manufacturing process. The higher microhardness of the material compared to pure copper in annealed state was attributed to the presence of Cu_2O oxides at grain boundary regions. The anisotropic microstructure originating from the layerwise deposition process resulted in slightly lower electrical conductivity and thermal diffusivity along the transversal direction compared to the building direction. However, the overall material exhibited physical properties comparable to pure copper standards.

The effective wall thickness of the printed membranes was significantly lower than the nominal values for all design settings, due to the presence of a porous surface layer not acting as a barrier for helium flow during leakage testing. This suggests the need to carefully account for dimensional deviations arising from the deposition process at the design stage and to further optimize the printing parameters to minimize the contribution of the porous surface layer to the overall membrane thickness. The 45° building orientation allowed achieving thicknesses closer to the design criteria. This was primarily attributed to the increased staircase effect and laser scanning length enabled by larger inclinations, resulting in the deposition of larger layers of compact material. Conversely, membranes produced with 67° and 90° orientations showed greater deviations from the design specifications and did not meet the tightness requirements for nominal thicknesses below 0.75 mm. The performance of these membranes was likely affected by residual porosity due to gas incorporation and incomplete powder melting during the printing process, which accounted for a significant fraction of the barrier thickness and is typically associated with vacuum degradation due to evacuation of trapped gases.

CRediT authorship contribution statement

Tobia Romano: Writing – review & editing, Writing – original draft, Methodology, Investigation, Data curation. **Andris Ratkus:** Writing – review & editing, Supervision, Resources, Project administration, Methodology, Funding acquisition, Conceptualization. **Samira Gruber:** Investigation. **Matteo Pozzi:** Resources, Investigation. **Hendrik Kos:**

Resources, Investigation. **Cedric Garion:** Resources, Investigation. **Samuel Rorison:** Validation, Investigation. **Elena López:** Resources, Project administration, Funding acquisition. **Toms Torims:** Supervision, Resources, Project administration, Funding acquisition, Conceptualization. **Maurizio Vedani:** Writing – review & editing, Supervision, Resources, Project administration, Funding acquisition, Conceptualization.

Declaration of competing interest

The authors declare that they have no known competing financial interests or personal relationships that could have appeared to influence the work reported in this paper.

Acknowledgements

This work was carried out as part of the I.FAST project within the framework of the European Union's Horizon 2020 Research and Innovation program under grant agreement No 101004730 and was supported by the Latvian Council of Science under grant agreement VPP-IZM-CERN-2022/1-0001.

Authors would like to acknowledge the support given by Nino Mori for elemental and spectrometry analyses and Dr. Giorgia Lupi for eddy current measurements. Dr. Tim Boot, Prof. Vera Popovich, and Dr. Richard Huizenga at the Department of Materials Science and Engineering of TU Delft are also aknowledged for hydrogen content measurements and X-ray diffraction analysis.

Data availability

Data will be made available on request.

References

[1] V. Dolgashev, S. Tantawi, Y. Higashi, B. Spataro, Geometric dependence of radio-frequency breakdown in normal conducting accelerating structures, Appl. Phys. Lett. 97 (2010), https://doi.org/10.1063/1.3505339.

[2] D. Gamzina, M. Kozina, A. Mehta, E.A. Nanni, S. Tantawi, P.B. Welander, T. Horn, C. Ledford, Copper reconsidered: material innovations to transform vacuum electronics, Proc. 20th Int. Vac. Electron. Conf. (2019) 1–2, https://doi.org/10.1109/IVEC.2019.8744750.

[3] T.J. Horn, D. Gamzina, Additive manufacturing of copper and copper alloys, Addit. Manuf. Process. (2020) 388–418, https://doi.org/10.31399/ASM.HB.V24.A0006579.

[4] P. Romanescu, D. Omidvarkarjan, J. Ferchow, M. Meboldt, Evaluation of the ultra-high vacuum suitability of laser powder bed fusion manufactured stainless steel 316L, Int. Conf. Addit. Manuf. Products Appl. (2024) 407–422, https://doi.org/10.1007/978-3-031-42983-5_27.

[5] D. Gamzina, N.C. Luhmann, C. Ledford, T. Horn, I. Karakaut, L. Lin, P. Frigola, Additive vacuum electronics: electron beam melting of copper, Proc. 18th Int. Vac. Electron. Conf. (2017) 1–2.

[6] L. Faillace, L. Palumbo, B. Spataro, A. Fukasawa, B.D. O'Shea, J.B. Rosenzweig, P. Frigola, Development of an ultra-high repetition rate S band RF gun for the SPARX project, in: Proc. IEEE Part. Accel. Conf., 2009, pp. 1815–1817.

[7] C.R. Wolf, F.B. Beck, L. Franz, V.M. Neumaier, 3D printing for high vacuum applications, in: Proc. 22nd Int. Conf. Cyclotrons Their Appl., 2020, pp. 318–321, https://doi.org/10.18429/JACoW-Cyclotrons2019-THC04.

[8] T. De Terris, T. Baffie, C. Ribière, Additive manufacturing of pure copper: a review and comparison of physical, microstructural, and mechanical properties of samples manufactured with Laser-Powder Bed Fusion (L-PBF), Electron Beam Melting (EBM) and Metal Fused Deposition Modelling (MFDM) technologies, Int. J. Mater. Form. 16 (2023), https://doi.org/10.1007/s12289-023-01755-2.

[9] Q. Jiang, P. Zhang, Z. Yu, H. Shi, D. Wu, H. Yan, X. Ye, Q. Lu, Y. Tian, A review on additive manufacturing of pure copper, Coatings 11 (2021) 740, https://doi.org/10.3390/coatings11060740.

[10] Y. Aghayar, P. Moazzen, B. Behboodi, A. Shahriari, S. Shakerin, A. Lloyd, M. Mohammadi, Laser powder bed fusion of pure copper electrodes, Mater. Des. 239 (2024) 112742, https://doi.org/10.1016/j.matdes.2024.112742.

[11] S. Gruber, L. Stepien, E. López, F. Brueckner, C. Leyens, Physical and geometrical properties of additively manufactured pure copper samples using a green laser source, Materials 14 (2021) 3642, https://doi.org/10.3390/ma14133642.

[12] T. DebRoy, H.L. Wei, J.S. Zuback, T. Mukherjee, J.W. Elmer, J.O. Milewski, A. M. Beese, A. Wilson-Heid, A. De, W. Zhang, Additive manufacturing of metallic components – process, structure and properties, Prog. Mater. Sci. 92 (2018) 112–224, https://doi.org/10.1016/j.pmatsci.2017.10.001.

[13] B. Brandau, A. Da Silva, C. Wilsnack, F. Brueckner, A.F.H. Kaplan, Absorbance study of powder conditions for laser additive manufacturing, Mater. Des. 216 (2022) 110591, https://doi.org/10.1016/j.matdes.2022.110591.

[14] M. Colopi, A.G. Demir, L. Caprio, B. Previtali, Limits and solutions in processing pure Cu via selective laser melting using a high-power single-mode fiber laser, Int. J. Adv. Manuf. Technol. 104 (2019) 2473–2486, https://doi.org/10.1007/s00170-019-04015-3.

[15] A.R. Gans, M.M. Jobbins, D.Y. Lee, S. Alex Kandel, Vacuum compatibility of silver and titanium parts made using three-dimensional printing, J. Vac. Sci. Technol. A. 32 (2014) 023201, https://doi.org/10.1116/1.4846195.

[16] J. Vovrosh, G. Voulazeris, P. Petrov, J. Zou, Y. Gaber, D. Woolger, M.M. Attallah, V. Boyer, Additive manufacturing of magnetic shielding and ultra-high vacuum flange for cold atom sensors, Sci. Rep. 8 (2018) 1–10, https://doi.org/10.1038/s41598-018-20352-x.

[17] A.P. Povilus, C.J. Wurden, Z. Vendeiro, M. Baquero-Ruiz, J. Fajans, Vacuum compatibility of 3D-printed materials, J. Vac. Sci. Technol. A. 32 (2014) 1–4, https://doi.org/10.1116/1.4873556.

[18] F. Grazzi, C. Cialdai, M. Manetti, M. Massi, M.P. Morigi, M. Bettuzzi, R. Brancaccio, F. Albertin, T. Shinohara, T. Kai, A. Fedrigo, A. Di Giovanni, F. Arneodo, R. Torres, O. Al-Ketan, J. Elhashemi, F. Taccetti, L. Giuntini, A multi-technique tomography-based approach for non-invasive characterization of additive manufacturing components in view of vacuum/UHV applications: preliminary results, Rend. Lincei 32 (2021) 463–477, https://doi.org/10.1007/s12210-021-00994-2.

[19] T. Romano, G. Pikurs, A. Ratkus, T. Torims, N. Delerue, M. Vretenar, L. Stepien, E. López, M. Vedani, Metal additive manufacturing for particle accelerator applications, Phys. Rev. Accel. Beams 27 (2024) 54801, https://doi.org/10.1103/PhysRevAccelBeams.27.054801.

[20] N. Cooper, L.A. Coles, S. Everton, I. Maskery, R.P. Campion, S. Madkhaly, C. Morley, J. O'Shea, W. Evans, R. Saint, P. Krüger, F. Oručević, C. Tuck, R. D. Wildman, T.M. Fromhold, L. Hackermüller, Additively manufactured ultra-high vacuum chamber for portable quantum technologies, Addit. Manuf. 40 (2021) 101898, https://doi.org/10.1016/j.addma.2021.101898.

[21] S. Jenzer, M. Alves, N. Delerue, A. Gonnin, D. Grasset, F. Letellier-Cohen, B. Mercier, E. Mistretta, C. Prevost, A. Vion, J.P. Wilmes, Study of the suitability of 3D printing for ultra-high vacuum applications, in: Proc. 8th Int. Part. Accel. Conf., 2017, pp. 3356–3358.

[22] S. Jenzer, M. Alves, S. Bilgen, J. Bonis, F. Brisset, S. Djelali, A. Gonnin, M. Guerrier, D. Grasset, F. Letellier-Cohen, Is it possible to use additive manufacturing for accelerator UHV beam pipes? J. Phys. Conf. Ser. 1350 (2019) 012199 https://doi.org/10.1088/1742-6596/1350/1/012199.

[23] R. Veness, W. Andreazza, D. Gudkov, A.M. Marin, S. Samuelsson, Metal 3D additive machining for in-vacuum beam instrumentation, Mech. Eng. Des. Synchrotron Radiat. Equip. Instrum. (2018) 121–124, https://doi.org/10.18429/JACoW-MEDSI2018-TUPH36.

[24] A. Speidel, L. Gargalis, J. Ye, M.J. Matthews, A. Spierings, R. Hague, A.T. Clare, J. W. Murray, Chemical recovery of spent copper powder in laser powder bed fusion, Addit. Manuf. 52 (2022) 102711, https://doi.org/10.1016/j.addma.2022.102711.

[25] A. Ratkus, T. Torims, G. Pikurs, V. Bjelland, S. Calatroni, R. Peacock, C. Serafim, M. Vretenar, W. Wuensch, M. Vedani, T. Romano, M. Pozzi, M.F. Pedretti, Initial high electric field – vacuum arc breakdown test results for additively manufactured pure copper electrodes, Proc. 14th Int. Part. Accel. Conf. (2023) 4957–4959, https://doi.org/10.18429/JACoW-IPAC2023-THPM030.

[26] G. Lanza, C. Nantista, D. Gamzina, C. Ledford, T. Horn, P. Carriere, P. Frigola, Outgassing of electron beam printed copper, Proc. 22nd Int. Vac. Electron. Conf. (2021), https://doi.org/10.1109/IVEC51707.2021.9722518.

[27] T. Torims, G. Pikurs, S. Gruber, M. Vretenar, A. Ratkus, M. Vedani, E. López, F. Brückner, First proof-of-concept prototype of an additive manufactured radio frequency quadrupole, Instruments 5 (2021), https://doi.org/10.3390/instruments5040035.

[28] T. Torims, A. Cherif, N. Delerue, M. Foppa Pedretti, S. Gruber, D. Krogere, E. Lopez, T. Otto, G. Pikurs, M. Pozzi, A. Ratkus, M. Thielmann, M. Vedani, M. Vretenar, P. Wagenblast, Evaluation of geometrical precision and surface roughness quality for the additively manufactured radio frequency quadrupole prototype, J. Phys. Conf. Ser. 2420 (2023), https://doi.org/10.1088/1742-6596/2420/1/012089.

[29] J.P. Fernández-Hernán, A.J. López, B. Torres, J. Rams, Influence of roughness and grinding direction on the thickness and adhesion of sol-gel coatings deposited by dip-coating on AZ31 magnesium substrates. A Landau–Levich equation revision, Surf. Coatings Technol. 408 (2021), https://doi.org/10.1016/j.surfcoat.2020.126798.

[30] P. Chiggiato, J.A. Ferreira Somoza, G. Bregliozzi, Criteria for Vacuum Acceptance Tests, CERN Technol, 2018. Depart. EDMS No.1752123.

[31] J. Metelkova, L. Vanmunster, H. Haitjema, D. Ordnung, J.-P. Kruth, B. Van Hooreweder, Hybrid dual laser processing for improved quality of inclined up-facing surfaces in laser powder bed fusion of metals, J. Mater. Process. Technol. 298 (2021) 117263, https://doi.org/10.1016/j.jmatprotec.2021.117263.

[32] A. Ulbricht, G. Mohr, S.J. Altenburg, S. Oster, C. Maierhofer, G. Bruno, Can potential defects in lpbf be healed from the laser exposure of subsequent layers? A quantitative study, Metals 11 (2021), https://doi.org/10.3390/met11071012.

[33] V. Candela, M. Pozzi, E. Chyhyrynets, V. Garcia Diaz, S. Candela, R. Dima, G. Favero, C. Pira, A. Pepato, P. Sonato, Smoothening of the down-skin regions of copper components produced via Laser Powder Bed Fusion technology, Int. J. Adv. Manuf. Technol. 123 (2022) 3205–3221, https://doi.org/10.1007/s00170-022-10408-8.

[34] Q. Jia, D. Gu, Selective laser melting additive manufacturing of Inconel 718 superalloy parts: densification, microstructure and properties, J. Alloys Compd. 585 (2014) 713–721, https://doi.org/10.1016/j.jallcom.2013.09.171.

[35] J. Yu, G. Wang, Y. Rong, Experimental study on the surface integrity and chip formation in the micro cutting process, Procedia Manuf. 1 (2015) 655–662, https://doi.org/10.1016/j.promfg.2015.09.063.
[36] X. Yan, C. Chang, D. Dong, S. Gao, W. Ma, M. Liu, H. Liao, S. Yin, Microstructure and mechanical properties of pure copper manufactured by selective laser melting, Mater. Sci. Eng. A 789 (2020) 139615, https://doi.org/10.1016/j.msea.2020.139615.
[37] L. Dong, F. Yang, T. Yu, N. Zhang, X. Zhou, Z. Xie, F. Fang, Contribution of grain boundary to strength and electrical conductivity of annealed copper wires, J. Mater. Res. Technol. 26 (2023) 1459–1468, https://doi.org/10.1016/j.jmrt.2023.08.012.
[38] T. Romano, M. Abdelwahed, S. Bengtsson, F. Bruzzo, R. Casati, H. Gedda, E. López, P. Ulfberg, C. Wilsnack, M. Vedani, Hybrid laser metal deposition of a Fe–Cr–Mo–V–Mn tool steel for hot stamping applications, Prog. Addit. Manuf. 8 (2023) 1241–1256, https://doi.org/10.1007/s40964-023-00396-w.
[39] G. Daurelio, M. Dell'Erba, L. Cento, Cutting copper sheets by CO2 laser, Lasers Appl. 5 (1986) 59–64.
[40] A. Ratkus, S. Rarison, C. Garion, H. Kos, S. Gruber, L. Stepien, A.A. Patil, E. Lopez, T. Torims, G. Pikurs, M. Vedani, V. Lacis, Evaluation of green laser source additive manufacturing technology for accelerator applications with ultra-high vacuum requirements, J. Phys. Conf. Ser. 2687 (2024), https://doi.org/10.1088/1742-6596/2687/8/082046.
[41] H. Rottländer, W. Umrath, G. Voss, Fundamentals of Leak Detection, Leybold GmbH, 2016. www.leybold.com.
[42] F. Grinschek, A. Charles, A. Elkaseer, C. Klahn, S.G. Scholz, R. Dittmeyer, Gas-tight means zero defects - design considerations for thin-walled fluidic devices with overhangs by laser powder bed fusion, Mater. Des. 223 (2022) 111174, https://doi.org/10.1016/j.matdes.2022.111174.
[43] J. Ding, S. Qu, L. Zhang, M.Y. Wang, X. Song, Geometric deviation and compensation for thin-walled shell lattice structures fabricated by high precision laser powder bed fusion, Addit. Manuf. 58 (2022) 103061, https://doi.org/10.1016/j.addma.2022.103061.
[44] S. Sgobba, Materials for high vacuum technology: an overview, CAS 2006 - cern Accel, Sch. Vac. Accel. Proc. (2007) 117–143.